

Segregated Chemistry and Structure on (001) and (100) Surfaces of $(\text{La}_{1-x}\text{Sr}_x)_2\text{CoO}_4$ Override the Crystal Anisotropy in Oxygen Exchange Kinetics

Yan Chen,^{†,‡} Helena Téllez,^{‡,§,‡} Mónica Burriel,^{‡,¶,‡} Fan Yang,^{||} Nikolai Tsvetkov,[†] Zhuhua Cai,[†] David W. McComb,^{||} John A Kilner,^{*,‡} and Bilge Yildiz^{*,†,⊥}

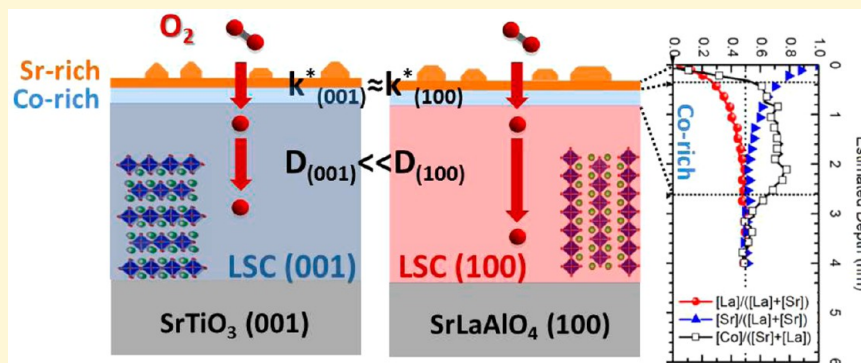
[†]Laboratory for Electrochemical Interfaces, Department of Nuclear Science and Engineering and [⊥]Department of Materials Science and Engineering, Massachusetts Institute of Technology, 77 Massachusetts Avenue, Cambridge, Massachusetts 02139, United States

[‡]Department of Materials, Imperial College London, Royal School of Mines, Exhibition Road, London SW7 2AZ, U.K.

[§]International Institute for Carbon Neutral Energy Research (wpi-I2CNER), Kyushu University, Nishi-ku, Fukuoka, Fukuoka 819-0395, Japan

^{||}Department of Materials Science and Engineering, The Ohio State University, Columbus, Ohio 43210, United States

Supporting Information



ABSTRACT: Attaining fast oxygen exchange kinetics on perovskite and related mixed ionic and electronic conducting oxides is critical for enabling their applications in electrochemical energy conversion systems. This study focuses on understanding the relationship between surface chemistry and the surface oxygen exchange kinetics on epitaxial films made of $(\text{La}_{1-x}\text{Sr}_x)_2\text{CoO}_4$, a prototypical Ruddlesden–Popper structure that is considered as a promising cathode material for fuel cells. The effects of crystal orientation on the surface composition, morphology, oxygen diffusion, and surface exchange kinetics were assessed by combining complementary surface-sensitive analytical techniques, specifically low energy ion scattering, X-ray photoelectron spectroscopy, Auger electron spectroscopy, scanning transmission electron microscopy, atomic force microscopy, and secondary ion mass spectroscopy. The films were grown in two different crystallographic orientations, (001) and (100), and with two different Sr compositions, at $x = 0.25$ (LSC25) and 0.50 (LSC50), by using pulsed laser deposition. In the as-prepared state, a Sr enriched layer at the top surface and a Co enriched subsurface layer were found on films with both orientations. After annealing at elevated temperatures in oxygen, the Sr enrichment increased, followed by clustering into Sr-rich secondary phase particles. Both the LSC25 and LSC50 films showed anisotropic oxygen diffusion kinetics, with up to 20 times higher oxygen diffusion coefficient along the ab -plane compared that along the c -axis at 400–500 °C. However, no dependence of surface oxygen exchange coefficient was found on the crystal orientation. This result indicates that the strong Sr segregation at the surface overrides the effect of the structural anisotropy that was also expected for the surface exchange kinetics. The larger presence of Co cations exposed at the LSC25 surface compared to that at the LSC50 surface is likely the reason for the faster oxygen surface exchange kinetics on LSC25 compared to LSC50. This work demonstrated the critical role of surface chemistry on the oxygen exchange kinetics on perovskite related oxides, which are thus far underexplored at elevated temperatures, and provides a generalizable approach to probe the surface chemistry on other catalytic complex oxides.

1. INTRODUCTION

1.1. Motivation. Over the past 20 years there has been a growing interest in the oxygen exchange kinetics of $(\text{ABO}_3)_2$ perovskite and perovskite related mixed conducting materials. This interest is because the exchange kinetics is critical in many

Received: June 18, 2015

Revised: June 29, 2015

Published: June 30, 2015

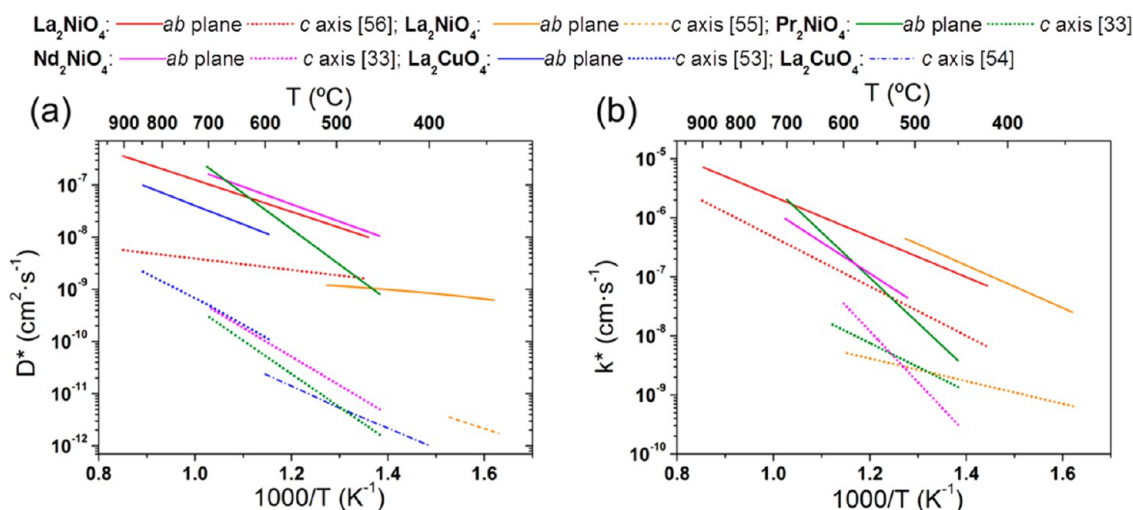


Figure 1. (a) Oxygen tracer diffusion coefficient, D^* , and (b) oxygen tracer surface exchange coefficient, k^* , along the ab -plane and c -axis direction reported in the literature for Ruddlesden–Popper 214 structured oxides.

of the important technological applications of these materials in clean energy conversion systems. These applications include electrodes for high temperature electrochemical devices,^{1–3} gas separation membranes,⁴ gas conversion/reformation catalysts,⁵ for information storage and processing by redox based resistive memories,^{6,7} and as active materials for sensors. Although the factors governing the oxygen self-diffusion in these materials are now fairly well understood,⁸ the exact mechanisms of the oxygen surface exchange process and their dependence on the surface structure remained elusive.^{9–11} Recent work on bulk and thin film materials has shown that the surfaces of these materials change markedly at operating temperatures due to cation segregation.^{12–22} In a number of recent studies the dominance of the AO termination of the perovskite ABO_3 (113) and the Ruddlesden–Popper (R–P) A_2BO_4 (214) has been seen at the outermost surface layer.^{23–26} These compositional changes can ultimately change the chemistry and phase composition, morphology, and electronic structure of the surface and were often associated with degradation of the oxygen exchange kinetics at the surface. Furthermore, these changes are time, temperature, and atmosphere dependent.^{16,27–29} It is clear that there is a need to understand and hence manage or eliminate these detrimental changes to aid in the durability of the devices mentioned above.

The motivation for this study was to investigate in detail the relationship between surface chemistry and the surface exchange process using a complementary multitechnique approach on well-defined epitaxial thin films. These films are made of $(La_{1-x}Sr_x)_2CoO_{4\pm\delta}$, a prototypical R–P structure that is considered as a promising fuel cell cathode, which exhibited interestingly fast oxygen exchange kinetics when interfaced with its perovskite counterpart $La_{1-x}Sr_xCoO_3$.^{30,31} Two different crystallographic orientations, (001) and (100), and two different Sr compositions, at $x = 0.25$ and 0.50 , were studied to assess the effects of orientation on the surface composition, morphology, and oxygen surface exchange and diffusion kinetics. There is some evidence in the literature that these 214 R–P materials have intrinsically anisotropic kinetic properties, with faster oxygen incorporation and diffusion along the rock-salt layers. However, the complexity of the surface chemistry may become an overriding factor to consider, hiding such intrinsically anisotropic and faster exchange kinetics

into the rock-salt layers, as will be revealed by our results in this paper.

1.2. Previous Results on Anisotropic Diffusion and Surface Reaction Kinetics in 214 R–P Oxides. There have not been a large number of studies on the anisotropy of the oxygen exchange kinetic parameters for $(La_{1-x}Sr_x)_2CoO_{4\pm\delta}$; however, there has been a considerable amount of literature on oxygen diffusion in related materials with the 214 R–P structure based on $(La_{1-x}Sr_x)_2CuO_{4\pm\delta}$ and $(La_{1-x}Sr_x)_2NiO_{4\pm\delta}$. This body of literature has been fully reviewed by Tarancon et al.³² with respect to their application as solid oxide fuel cell (SOFC) cathodes and recently complemented by the work by Bassat et al.³³ on Pr_2NiO_4 and Nd_2NiO_4 . Thus, we will restrict this section to a brief overview of the prior work that has been done to investigate the anisotropy in both the diffusion coefficient and the surface exchange coefficient in 214 R–P oxides. One major factor to consider when reviewing these materials is that the nature of the dominant oxygen defect can change depending upon the level of substitution by strontium. For low strontium substitutions the dominant oxygen defect is an oxygen interstitial ion but for high strontium substitution this changes to an oxygen vacancy. For the stoichiometry under consideration here ($x = 0.25$ and 0.5 in $(La_{1-x}Sr_x)_2CoO_{4\pm\delta}$) oxygen interstitials are the majority defects in air,^{34,35} and thus we will focus on this regime.

There have been a number of simulations of oxygen migration in the 214 R–P oxides.^{36–48} Perhaps the most relevant of these is a recent paper dealing with molecular dynamics (MD) simulation of interstitial migration in $La_{1.2}Sr_{0.8}CoO_{4.1}$ by Tealdi et al.⁴⁸ As with previous MD simulations of 214 materials,^{45,47} they showed that the oxygen interstitials and the apical oxygen ions on the CoO_6 octahedra are involved in an interstitialcy mechanism confined to the $(La,Sr)_2O_2$ layers with an activation energy of 0.71 eV. This gives a predicted anisotropy of the oxygen diffusion, although Tealdi et al.⁴⁸ did not give a value for the c -axis diffusion because it was not observed during the MD simulations. Lattice static calculations of the unsubstituted La_2CoO_{4+d} again show the interstitialcy mechanism to be dominant and reported a large difference in the activation energy parallel to (0.73–0.80 eV) and perpendicular to (1.37–1.39 eV) the La_2O_2 planes.⁴⁴

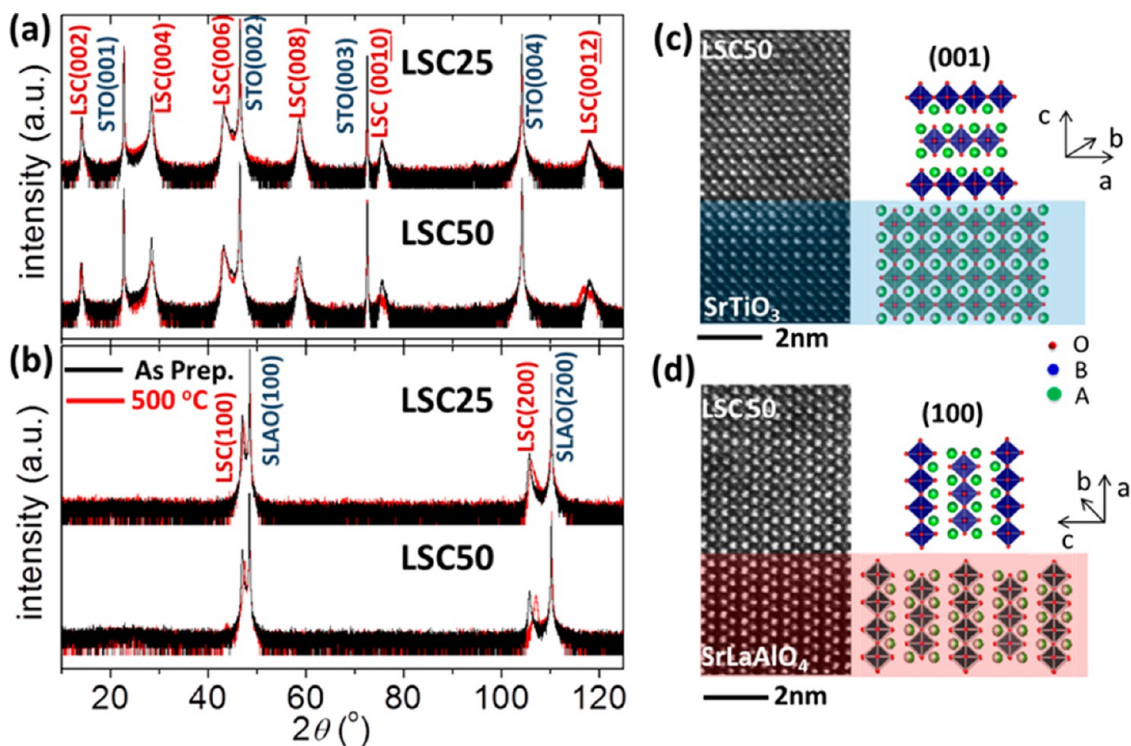


Figure 2. (a-b): X-ray diffraction 2θ - ω scans of (a) LSC25 (001) and LSC50 (001) films on SrTiO_3 (001) and (b) LSC25 (100) and LSC50 (100) films on SrLaAlO_4 (100), in their as-prepared state (black data) and after annealing at 500 °C in 200 mbar O_2 for 10.25 h (red data). (c-d) Representative scanning transmission electron microscopy high-angle annular dark field (STEM-HAADF) images of the cross-section of (c) LSC50 (001) on SrTiO_3 (001) and of (d) LSC50 (100) on SrLaAlO_4 (100). In (d) the interface can be identified due to the differences in atomic number of the B-site cations. The crystal structure of the films and substrates are visualized using the Vesta software,⁵⁸ and the red, blue, and green spheres represent the oxygen, B-site, and the A-site cations of the film and substrate compositions.

Simulations of the interaction of molecular oxygen with the surface of the 214 materials are more limited with only two recent works using density functional theory (DFT) simulations of perfect and defective surfaces of $\text{La}_2\text{NiO}_{4+\delta}$ ⁴⁹ and of $(\text{La}_{1-x}\text{Sr}_x)_2\text{CoO}_{4+\delta}$.³⁴ The authors chose the (100) and (001) surfaces for their simulation and showed that the surface Ni and Co atoms are very important for the adsorption of the oxygen molecule. The importance of transition metal cations in the reactions involving oxygen is recognized also on several other perovskite oxides.^{50–52} On the other hand, recent surface analysis of these materials throws doubt on the full presence of the transition metal cation at the surface.^{24,26} As will be shown in this work, segregation of Sr to the top surface can block the exposure of the transition metal cations to the oxygen gas and inhibits the oxygen exchange reactions at the gas–solid interface. In refs 34 and 49 the authors also showed that defective surfaces are more reactive and that the oxygen vacancies should be involved with the adsorption and reduction of oxygen molecules at the surface. While in $\text{La}_2\text{NiO}_{4+\delta}$ ⁴⁹ the authors did not give any indication in the expected anisotropy of this process as only one surface was considered, in $(\text{La}_{1-x}\text{Sr}_x)_2\text{CoO}_{4+\delta}$ ³⁴ the authors predicted 100 times faster oxygen chemical incorporation kinetics on the (100) surface compared to the (001) surface.

Contrary to the theoretical studies there is a significant body of experimental results showing the anisotropy in the diffusion and surface exchange for R–P oxides, determined by the isotope exchange depth profiling (IEDP) method. This data is summarized in Figure 1 with data from single crystals of La_2CuO_4 ,^{53,54} Pr_2NiO_4 ,³³ and Nd_2NiO_4 ³³ and from single

crystals⁵⁵ and epitaxial thin films⁵⁶ of La_2NiO_4 . An anisotropy (temperature dependent) of ca. 2 orders of magnitude is apparent in the tracer diffusion coefficients, D^* , shown in Figure 1 (a). The anisotropy for the surface exchange coefficients, k^* , shown in Figure 1 (b) is less strong than that for diffusion. The largest anisotropy in k^* is for the La_2NiO_4 thin film work of Burriel et al.⁵⁶ which is close to a factor of 100; however, the data of Bassat⁵⁵ shows a lower value. One point to note here is that for measurements of anisotropy performed on oriented single crystals, there is a limit to the extent of anisotropy that can be captured by this technique because of the accuracy to which the crystals can be oriented and cut.⁵⁷ Similar limitations apply to measurements made in individual grains of ceramics where the orientation has been determined by EBSD.⁵³ Thus, most measurements of the diffusion in the slower c -direction probably represent an upper limit (because of mixing with the ab -diffusion). The determination of the surface exchange coefficient is subject to larger errors than the diffusion coefficient.

2. EXPERIMENT METHODS

$(\text{La}_{1-x}\text{Sr}_x)_2\text{CoO}_4$ with two different Sr doping levels, $(\text{La}_{0.75}\text{Sr}_{0.25})_2\text{CoO}_4$ (LSC25) and $(\text{La}_{0.5}\text{Sr}_{0.5})_2\text{CoO}_4$ (LSC50), were grown by Pulsed Laser Deposition (PLD). PLD was carried out at 700 °C with O_2 pressure (P_{O_2}) of 10 mTorr. The laser beam energy was set at 400 mJ per pulse, and the pulse frequency was 10 Hz. After deposition, the samples were cooled to room temperature with a cooling rate of 5 °C/min under 2 Torr oxygen pressure. Single-crystal SrTiO_3 (001) (STO, $a = c = 3.905$ Å) and SrLaAlO_4 (100) (SLAO, $a = 3.756$ Å, $c = 12.636$ Å) (MTI Corporation, Richmond, CA) were used as the substrates to produce LSC25 and LSC50 films with (001)

Table 1. LSC25 and LSC50 Samples, Heat Treatment Conditions, and Analysis Techniques Presented in This Work

samples	heat treatment for each sample	analysis for each sample
LSC25 (001)/SrTiO ₃	as-prepared	cation composition: LEIS (outmost surface to near surface), XPS (near surface), and depth profiling
LSC25 (100)/SrLaAlO ₄	400 °C, 200 mbar O ₂ (with <1 wppm water content), for 10.25 h	surface structure and phase separation: AFM (surface structure), AES (local composition with lateral resolution at the surface)
LSC50 (001)/SrTiO ₃	500 °C, 200 mbar O ₂ (with <1 wppm water content), for 10.25 h	bulk structure: HR-XRD (orientation and lattice constant)
LSC50 (100)/SrLaAlO ₄		composition and atomic structure: STEM/EDS oxygen exchange and diffusion kinetics: SIMS (with ¹⁸ O tracer)

and (100) crystal orientations, respectively. These different compositions and orientations are referred to as LSC25 (001), LSC25 (100), LSC50 (001), and LSC50 (100) in the rest of the paper. Two sets of samples were prepared: thin films with the thickness of 39–45 nm and thick films with the thickness of 81–84 nm. All the results presented in the main text are for the thin films unless specified. The thicker films gave consistent results, which are shown in the [Supporting Information](#).

The crystal structure of samples were measured by high resolution X-ray diffraction (HR-XRD), which used a high resolution four circle Bruker D8 Discover diffractometer, with a Göbel mirror, four-bounce Ge(022) channel-cut monochromator, Eulerian cradle, and a scintillation counter, using Cu K α 1 radiation. The HRXRD results showed that the LSC25 and LSC50 films grown on STO and SLAO substrates exhibited only the (001) and (100) diffractions ([Figure 2 \(a–b\)](#)), respectively. The (001) films on STO are with the *ab*-plane parallel to the surface and *c*-axis perpendicular to the surface, while (100) films on SLAO are with their *c*-axis parallel to the surface, as shown in [Figure 2 \(c–d\)](#).

The surface chemistry, structure of the films with different doping levels, and crystal orientations were compared in their as-prepared state and after annealing at different temperatures in 200 mbar O₂ gas environment with less than 1 wppm water content (see [Table 1](#)).

The surface and near-surface chemical composition was investigated by low-energy ion scattering spectroscopy (LEIS) using a Qtac100 spectrometer (ION-TOF GmbH, Münster, Germany). Uniquely, this technique provides elemental information on the outermost layer of atoms by analyzing the kinetic energy distribution of noble gas ions backscattered from the surface.⁵⁹ Different analytical beams (i.e., typically 3 keV He⁺ and 5 keV Ne⁺ beams) can be provided by a high brightness plasma source, impacting the surface at normal incidence. The scattered primary ions are collected for all azimuthal angles at a scattering angle of 145°, and the resultant energy spectrum can be related to the elemental (and isotopic for light elements) composition according to the kinematics of the scattering event. The primary ion beam is rastered over a large area (typically 1 mm²) while keeping the ion fluence below $\sim 5 \times 10^{13}$ ions cm⁻² to avoid significant surface damage during the spectrum acquisition. Due to the extremely high surface sensitivity of the LEIS technique, the samples were in situ cleaned after being loaded into the instrument in order to remove any contamination. The details of the surface cleaning procedure are provided in [Supporting Information S1](#).

The low-energy sputtering source is used for depth profiling analysis in order to determine the near-surface cation distribution (up to a depth of ~ 10 nm). This source provides an Ar⁺ beam that impacts in a pulsed mode at 59° to the surface normal, alternating with the primary beam analysis cycle during the dual-beam depth profiling. The sputtered area is 1.5×1.5 mm². The cation surface coverages were estimated by using a back-calibration procedure assuming that the cation plateau signals at the end of the depth profile correspond to the bulk stoichiometric values, following the procedure described elsewhere.^{26,60}

The near surface chemistry was also studied by angle resolved X-ray photoelectron spectroscopy (XPS), using the PerkinElmer PHI-5500 ESCA spectrometer with monochromated Al K α (1486.65 eV) X-ray radiation equipped with charge neutralization. The cation compositions on the samples were quantified based on the La 3d, Co 2p, and Sr 3d peaks using the CasaXPS software. The spectra were taken at

three photoelectron emission angles, 90°, 45°, and 20°, with increasing sensitivity to the surface at lower emission angles. The probing depth, estimated as three times the inelastic mean free path of photoelectrons (3 \times IMFP), at 90° was about 8, 5, and 5 nm for Sr 3d, La 3d, and Co 2p, respectively. Changing the emission angle to 45° and 20° decreases the probing depth down to 71% and 34%, respectively, of that at 90°. The binding energies were calibrated using the C 1s peak at 284.8 eV as the internal reference peak.

A Veeco/Digital Instrument Nanoscope IV was used to perform tapping mode atomic force microscopy (AFM) for characterizing the surface morphology. AFM images were processed using the Nanoscope software version 5.31R1 (Digital Instruments).

A Physical Electronics Model 700 scanning nanoprobe Auger electron spectroscopy (AES) instrument was used to detect lateral heterogeneities in cation compositions with high spatial resolution. Electron beam settings of 20 keV and 10 nA were used for both SEM imaging and the Auger electron excitation. The La MNN, Sr LMM, and Co LMM Auger emissions were measured for quantifying the surface cation composition of the LSC films. The smoothing and differentiation of the AES spectra collected were carried out using the Savitsky–Golay algorithm. Quantification of the AES differential spectra is performed using peak-to-peak intensities of the tight-scans of the noted emissions from the constituent cations. The probing depths (3 \times IMFP) are about 8.0 nm for Sr LMM, 4.0 nm for La MNN, and 4.5 nm for Co LMM emissions. We used the standard sensitivity factors (Physical Electronics Inc., 2006) for the chemical quantification with AES, and the actual sensitivity factors for these emissions in the LSC25 and LSC50 films may vary from the provided standards. Therefore, rather than the absolute values of the surface chemical content, the qualitative trends should be taken into account regarding the AES results.

The scanning transmission electron microscopy (STEM) samples were prepared with a Helios NanoLab 600 dual-beam focused ion beam (FIB) instrument. In order to prevent any ion beam damage to the surface, all samples were capped with approximately 100 nm of Au layer prior to FIB milling. High resolution STEM images were taken on an FEI aberration (probe)-corrected Titan 80-300 instrument operated at 300 kV. A high-angle annular dark field (HAADF) detector was used to obtain image contrast that is predominantly incoherent. This is commonly referred to as *Z*-contrast imaging as the intensity of scattering from each resolved atomic column depends strongly on the atomic number (approaching $\sim Z^2$).^{61,62} X-ray energy dispersive spectroscopy (EDS) was performed on an FEI aberration (image)-corrected Titan G2 60-300 equipped with a quad silicon drift detector. All the EDS analyses were carried out by the Cliff–Lorimer method using experimental *k*-factors obtained by using the bulk film as an internal standard of stoichiometry as in LSC50.

In order to evaluate the orientation dependence of the oxygen diffusion and surface exchange properties of the LSC films, isotopic exchange experiments were performed using the same methodology as described in [ref S6 \(Supporting Information S2\)](#). Prior to the exchange, the films were annealed at the testing temperature in research grade ¹⁶O₂ (>99.9995%) to ensure that equilibrium was established. Short ¹⁸O exchanges (between 10 and 45 min) were performed on uncovered LSC50 and LSC25 thin films (39–45 nm) over the temperature range of 290–575 °C using the transverse configuration (oxygen diffusion perpendicular to the film plane) to evaluate their surface exchange properties (see [Figure S1\(a\)](#)). For each

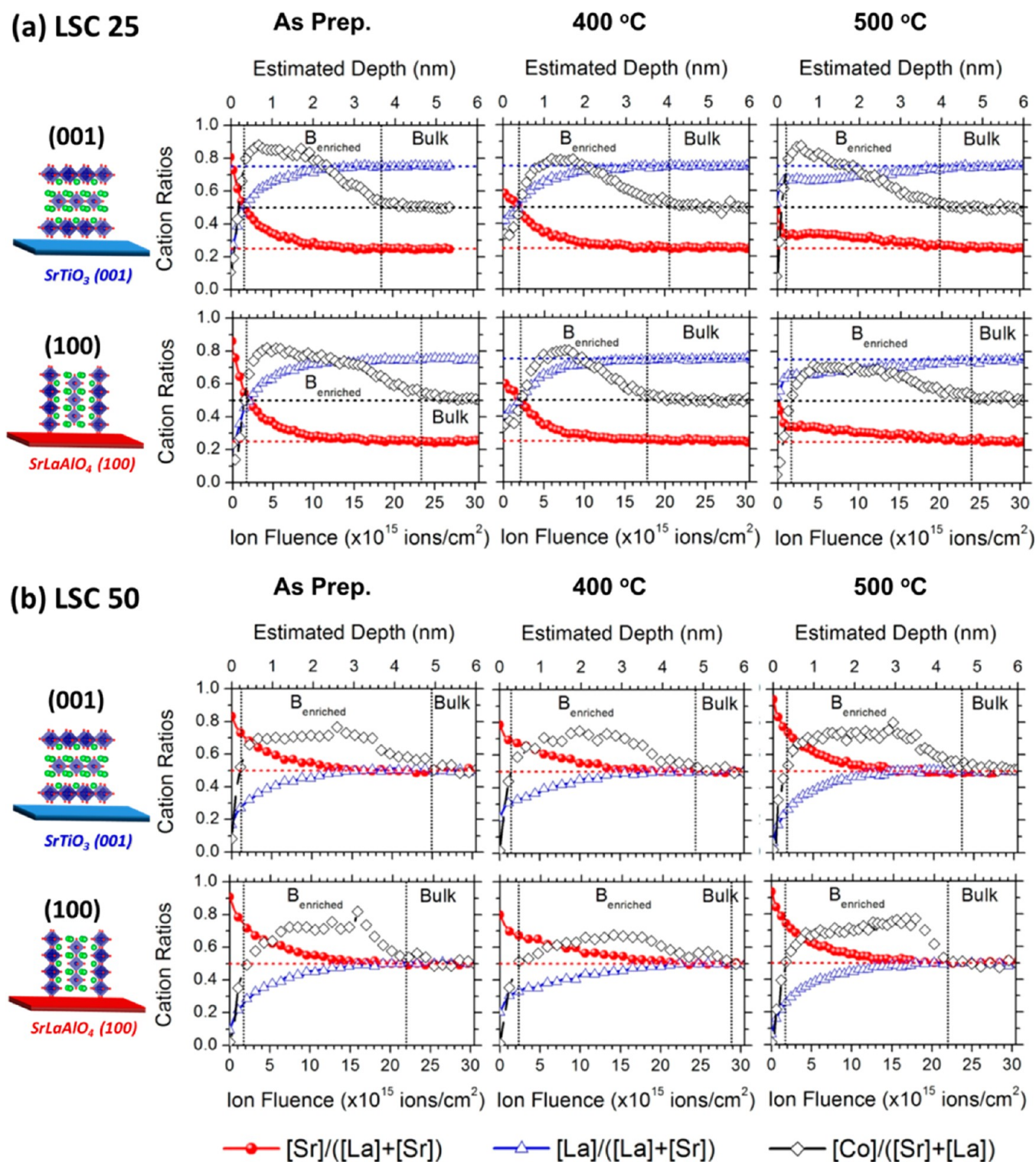


Figure 3. Cation compositions deduced from LEIS for (a) LSC25 and (b) LSC50 films with (001) orientation (top row) and (100) orientation (bottom row) for each. The depth profiles show the surface and near-surface restructuring as a function of the thermal history of the films (left to right, as-prepared, 400 and 500 °C for 10.25 h).

of the temperatures, the oxygen exchange was always carried out simultaneously on two samples of the same composition with two different orientations (001) and (100). In order to evaluate the oxygen diffusion in the transversal configuration, thicker samples were required. Therefore, an additional exchange was carried out for 85 min at 500 °C for the thick LSC50 films (81–84 nm). In the case of the LSC25, another exchange was carried out for 65 h at approximately 500 °C on two thin (001) and (100) films using the longitudinal

configuration (oxygen diffusion parallel to the film plane) (see Figure S1(b)). In this case the films had been previously covered with a dense and uniform Au thin film, which prevents oxygen exchange from the top surface, and a trench had been opened using a diamond tip to allow oxygen exchange from the side of the trench. All the exchanged samples were measured by time-of-flight SIMS (ToF-SIMS) on a ToF-SIMS machine (ION-TOF GmbH, Münster, Germany) equipped with a bismuth LMIG pulsed gun incident at 45°. A 25 keV Bi⁺

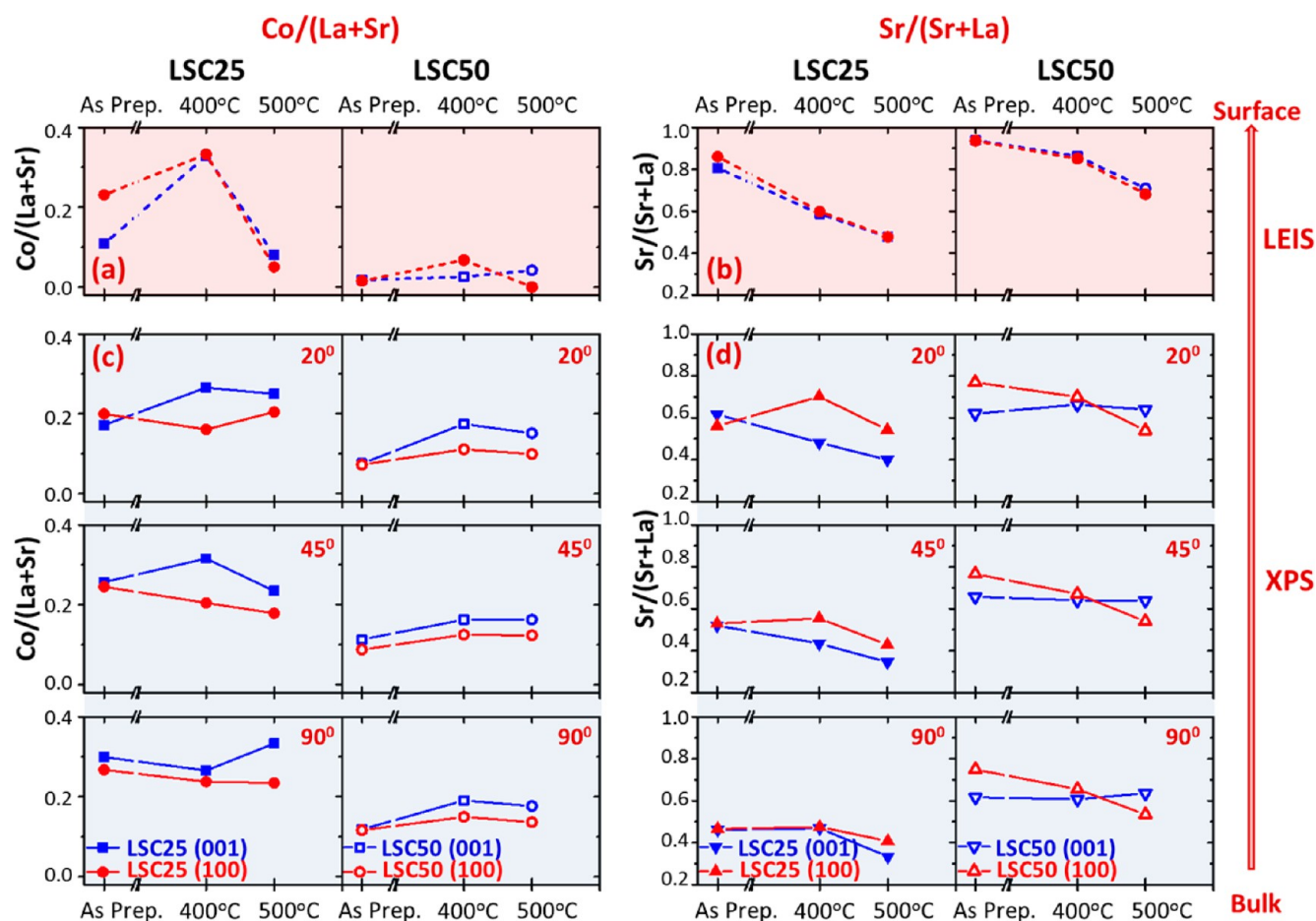


Figure 4. Comparison of Co/(La+Sr) and Sr/(Sr+La) quantified by LEIS and XPS for LSC25 (001) and (100) and for LSC50 (001) and (100) films: (a) Co/(La+Sr) and (b) Sr/(La+Sr) from the top surface quantified by LEIS; (c) Co/(La+Sr) and (d) Sr/(La+Sr) quantified by XPS, with photoelectron emission angles at 20°, 45°, and 90°, corresponding to the probing depths ($3 \times \text{IMFP}$ of photoelectrons) from near surface ($\sim 2\text{--}3$ nm) to the bulk ($\sim 5\text{--}8$ nm), respectively.

primary ion beam was used to generate the secondary ions using burst alignment mode (eight pulses) for analysis and a Cs^+ beam (2 keV) incident at 45° for sputtering. For each exchanged sample the distribution of the oxygen isotopes (^{18}O and ^{16}O) as well as other characteristic relevant secondary ion species, LaO^- , SrO^- , CoO^- (for the film), in addition to TiO^- and LaO^- (for the substrates) samples were acquired in selected regions. More details on the ^{18}O exchange depth profiling experiment can be found in [Supporting Information S2](#).

3. RESULTS AND DISCUSSION

3.1. Segregated Surface Chemistry. **3.1.1. Composition Profile from Outmost Surface to Bulk Quantified by LEIS.** The LSC thin films were analyzed in as-prepared condition and after annealing and isotopic exchange treatments described previously ([Table 1](#)) in order to investigate the cation segregation that takes place during the PLD deposition process itself and during the thermal annealing.

The outermost surfaces of the as-prepared films show predominant coverage of the surface by Sr for all the compositions and orientations, with a higher Sr coverage for the LSC50 compared to the LSC25 (first point of LEIS depth profiles in [Figure 3](#)). Also see [Supporting Information Figure S2](#) for the surface spectra. This surface termination indicates that the Sr cations segregate during the PLD deposition ([Figure 3](#), depth profiles of the as-prepared samples). This behavior is in agreement with previous LEIS studies on perovskite and

perovskite-related materials, which showed preferential segregation of the divalent cations.^{12,29} Annealing of the films at 400 and 500 °C gave rise to a mixed La–O and Sr–O dominated surface, with only a small amount of transition metal, Co, detected on the outer surface for any of the LSC compositions or orientations under study. An apparent decrease of the Sr while an increase of the La was observed ([Figure S2](#) dashed lines, [Figure 4](#) (a–b), and color bar in [Figure 5](#)). These results might seem contradictory to the increased Sr segregation that may be expected upon annealing. However, as it will be evident later in this paper, we attribute the apparent decrease of the Sr surface coverage to the formation of Sr-rich particles that cluster at the surface (more detailed discussion in [section 3.2](#)).

LEIS depth profiling demonstrated that the Sr cations segregate toward the surface preferentially over the La cations, whereas the Co cations are located below the outer surface ([Figure 3](#)). This behavior is similar to recent results on polycrystalline perovskite-related materials.²⁶ Furthermore, the depth profiles here show that the layered R–P LSC films undergo restructuring at the near-surface region, with a Co-enriched region at an estimated depth of around 2–5 nm. The Co/(Sr+La) ratios underneath the Sr-enriched surface layer are larger than those corresponding to a 214 R–P phase ($(\text{B:A ratio})_{214} = 0.5$). According to the Co/(Sr+La) ratios (>0.5) obtained at the near surface region, these Co-enriched phases may correspond to a different stacking sequence with more

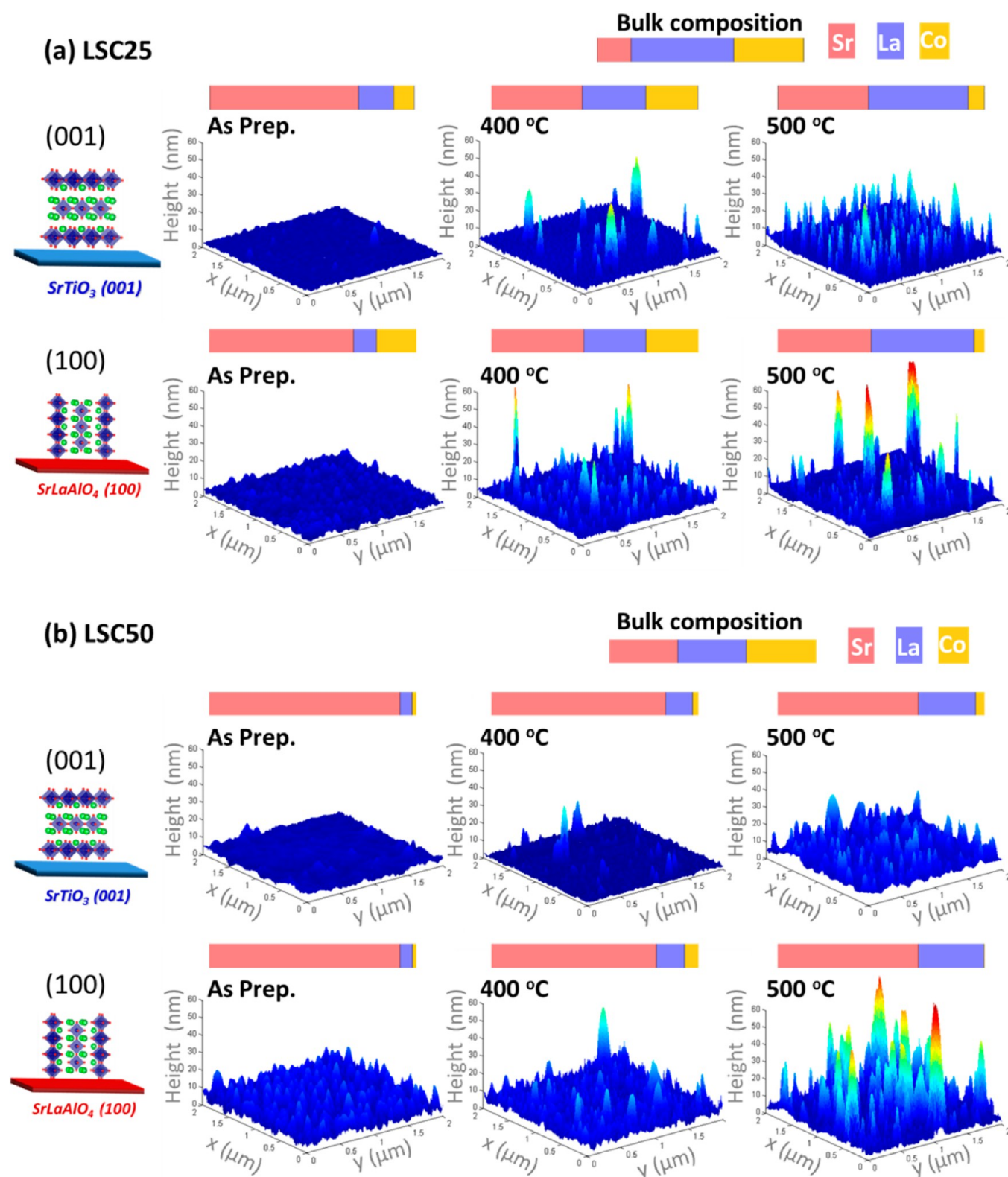


Figure 5. Surface topography (3D image) characterized by AFM and the cation composition of the outermost surface composition quantified by LEIS (the color bar on top of each AFM figure), for LSC25 (a) and for LSC50 (b), in their as-prepared state and after annealing at 400 and 500 °C in O₂ for 10.25 h.

perovskite layer in the structure ($A_{n+1}B_nO_{3n+1}$ $n > 1$), similarly to those found previously on LNO single crystals.⁶³ The thicknesses of the higher order R–P phases increased with higher annealing temperatures due to the increased amount of Sr-segregation out to the surface, as observed in Figure 3 and

Supporting Information Figure S3. The Co enriched layer in LSC50 was thicker than that in LSC25, which is consistent with more Sr segregation at the surface of LSC50.

The LEIS results here and the XPS, AFM, and Auger results shown in the later sections were all obtained from the thin films

with 39–45 nm thickness. The sample sets with 81–84 nm film thickness showed consistent results (seen in Figure S3) as the thin ones.

3.1.2. Near Surface Chemistry Quantified by XPS. Angle resolved XPS was also used, complementarily to LEIS, to quantify the chemical composition from the near surface with different probing depths for the LSC25 and LSC50 films with the (100) and (001) orientations in their as-prepared states and after annealing, as shown in Figure 4. Figure 4 (a) and (b) shows the outermost surface composition of LSC25 and LSC50 quantified from LEIS, for comparison to XPS near-surface results shown in Figure 4 (c) and (d). The relative presence of B-site versus A-site cations (quantified as $\text{Co}/(\text{Sr}+\text{La})$) in Figure 4 (c)) and Sr fraction at the A-site (quantified as $\text{Sr}/(\text{Sr}+\text{La})$ in Figure 4 (d)) were assessed by analyzing the Sr 3d, La 3d, and Co 2p photoelectron emissions at 90°, 45°, and 20° emission angles. We also recall here that, even though we vary the relative depth sensitivity by varying the emission angle, by its nature the XPS data is always exponentially more sensitive to the near-surface region, even in the data coming from 90° with the deepest probing depth. Therefore, the composition data in Figure 4 (c) and (d) as a function of emission angle should be interpreted as a *trend* but not as a quantified composition for a specific depth (angle).

It can be seen from Figure 4 (c) that the $\text{Co}/(\text{Sr}+\text{La})$ ratios for both LSC25 and LSC50 films are less than 0.5 for all the samples. This means that the surface is Co-deficient on all the samples. The results for measurements with photoelectron emission angles of 90°, 45°, and 20° are compared in Figure 4 (c) and (d). As the probing depth decreases (from bulk toward the surface), the $\text{Co}/(\text{Sr}+\text{La})$ ratios decrease. This trend indicates that such Co deficiency is more prominent at the top surface. As shown in Figure 4 (c), the (100) films presents slightly lower $\text{Co}/(\text{Sr}+\text{La})$ ratios than the (001) films, for both LSC25 and LSC50. The $\text{Sr}/(\text{Sr}+\text{La})$ values for both LSC25 and LSC50 films (Figure 4 (d)) are larger than the bulk composition, which are 0.25 and 0.5 for LSC25 and LSC50, respectively. As the probing depth decreases (from bulk toward the surface), the $\text{Sr}/(\text{Sr}+\text{La})$ ratio increases. These results indicate that Sr segregation toward the surface is more than La, although both La and Sr are apparently increasing toward the surface. The Sr/La ratios seem to decrease with annealing temperature, as shown in Figure 4 (b) and (d) for LEIS and XPS results. Such apparent decrease is considered to be due to the clustering of Sr enriched particles at the surface and is not an indication of a lowering of Sr segregation to the surface, which will be discussed more in section 3.2.

3.1.3. Comparison of the LEIS and XPS Results for Cation Composition at/near the Surface. We can see that the $\text{Co}/(\text{La}+\text{Sr})$ and $\text{Sr}/(\text{Sr}+\text{La})$ ratios quantified by XPS in 3.1.2 and ones from LEIS in 3.1.1 are qualitatively consistent with each other. Both measurements showed that the surface of the LSC films is Co-deficient regardless of orientation and composition and that the relative presence of Co at surface of LSC25 is more than that at LSC50. Furthermore, surface Sr enrichment was found in both LEIS and XPS measurement. The $\text{Sr}/(\text{Sr}+\text{La})$ ratio at the outmost surface quantified by LEIS (Figure 4 (b)) appears to be higher than that at the near-surface (20°) quantified by XPS (Figure 4 (d)), which confirms that the most extensive Sr segregation is at the top surface. Both the LEIS and the XPS signatures indicated that the Sr signal from the surface decreased with annealing temperature. However, both LEIS and XPS are laterally averaging techniques, without any spatial

resolution of chemical heterogeneities at the surface. Therefore, if Sr enrichment is accompanied by clustering into secondary phases and dewetting of the surface, LEIS and XPS that skims the surface in a laterally averaged manner cannot capture the total quantity of Sr that is accumulating and separating out of the base phase in a heterogeneous manner at the surface. Section 3.2 below presents such lateral heterogeneities and the evidence to the actual increase of Sr segregation with increasing temperature.

3.2. Segregated Surface Structure and Phase Separation.

3.2.1. Surface Topography Characterized by AFM. The LEIS and XPS results showed that, after annealing at 400–500 °C in O_2 , the Sr content at the top surface decreased, while the Co content increased. To understand the reason for this behavior, the morphology of the films was studied by AFM. Figure 5 shows the surface topography of LSC25 and LSC50 films in the as-prepared states (left) and after annealing at 400 °C (middle) and 500 °C (right) in O_2 for 10.25 h. On top of each AFM image, the colored bar chart represents the corresponding outermost surface composition of the same sample quantified by LEIS. As a reference for comparison, the bar chart for the bulk nominal composition of LSC25 and LSC50 is also shown at the top of Figure 5 (a) and (b). After annealing in O_2 , the surface of both LSC25 and LSC50 films became rougher, because of the formation of particles at the surface (see Figure S2 for the AFM images). We identified that these particles are Sr-enriched phases by AES measurements, which will be shown in the following section 3.2.2.

As shown in Figure 5 (a) and (b), the surfaces of LSC50 are rougher than that of LSC25. The surface roughness increases with annealing temperature (Figure S5 (a)). Due to the higher level of Sr segregation on LSC50 films, the roughness on LSC50 is larger than LSC25 for both orientations. The average surface coverage of the particles was also analyzed, as shown in Figure S5 (b). The larger roughness on LSC50 is a result of the larger size and coverage of the particles at the surface. For LSC50, there are more particles on the surface of the (100) oriented film than that on (001) oriented one.

As shown in Figure 5 and Figure S4, the Sr segregation at the surface is accompanied by the formation of particles at the surface after annealing at high temperature in O_2 . As will be seen in the next section 3.2.2, these particles are made of Sr-rich oxides. The average height of these particles is on the order of 10 nm, and many particles are as high as tens of nm, beyond the probing depth of LEIS and XPS without sputtering. Therefore, the amount of Sr at the surface measured by XPS and LEIS is an underestimate as a result of such clustering of Sr-rich secondary phases.

The average height of particles observed by AFM on the annealed LSC25 and LSC50 films (~10 nm) appears larger than the depth of the Sr enriched layer (<6 nm) identified by the LEIS depth profiling (Figure 3). As will be shown by the results from AES and STEM analysis (section 3.2.2 and section 3.2.3), we have identified the Sr rich particles to be SrO_2 , a phase that is stable only up to 800 K and unstable under electron beam (Figure S6). Therefore, it is possible that the sputtering of these relatively unstable particles by Ar^+ ions during the LEIS depth profiling process is faster than the particle-free zones of the base LSC film. This preferential sputtering of the particles can give rise to a seemingly thinner Sr segregation layer than the size of these Sr-rich particles.

3.2.2. Composition of Surface Phases Quantified by Nanoprobe AES. To examine the chemical composition of

the segregated particles observed by AFM (Figure 5) at the surface of the LSC25 and LSC50 films, we performed AES analysis with ~ 10 nm resolution coupled with SEM imaging. The SEM image and the corresponding elemental maps deduced by AES on the LSC25 (100) film annealed at 500 °C are given as an example in Figure S7. It is clear that the particle regions which have high Sr content correspond to lower Co and La levels at the surface. Figure 6 (a-b) shows the

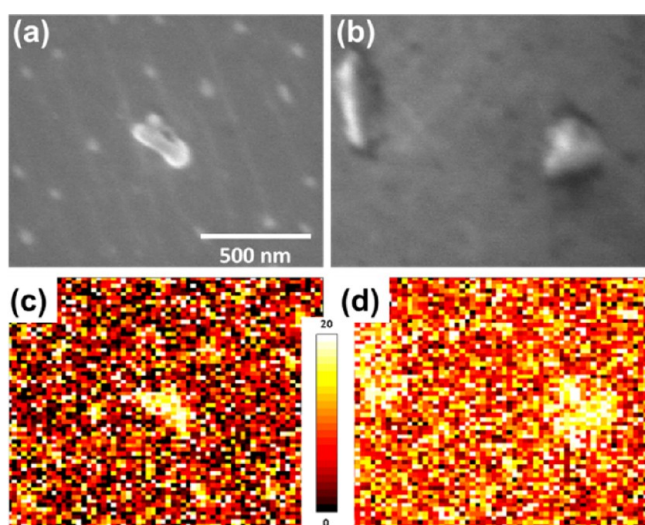


Figure 6. (a-b) Scanning electron microscopy image of the LSC25 (100) (a) and LSC50 (100) (b) after annealing at 500 °C for 10.25 h and (c-d) corresponding Sr/Co composition ratio maps deduced by AES for LSC25(100) (c) and LSC50(100) (d). The scale bar reflects Sr/Co cation ratio variations.

SEM images of the LSC25 (100) and LSC50 (100) films, and the corresponding Sr/Co composition ratio maps deduced by AES are shown in Figure 6 (c-d) after annealing at 500 °C in

O₂ for 10.25 h. The particles are larger on the LSC50 compared to the LSC25 films, consistent with the AFM analysis presented in Figure 5 and Figure S5.

Using the results of the AES analysis we estimated the relative variations in the Sr/Co across the surfaces of the LSC25 (100) and LSC50 (100) films (Figure 6 (c-d)). On both compositions, the significant increase in the Sr/Co is evident for the particles compared to the particle-free zones of the surface. This result is in line with our previous observations on La_{1-x}Sr_xCoO₃²⁷ and La_{1-x}Sr_xMnO₃¹⁹ by using the same technique, suggesting that the segregated particles are made largely of SrO_x or related compounds, accompanied by small amounts of La-oxide, Co-oxide, or La-Co-oxide. The mechanisms behind the Sr enrichment at the perovskite oxide surfaces, based on electrostatic and elastic interactions, are also discussed in detail in our previous report.¹⁹

Because of the insulating nature of SrO_x, we and others in the literature think that the segregated Sr-rich particles do not participate in oxygen exchange process and block the surface.^{21,64} In order to evaluate the effect of nominal Sr content in LSC films on the oxygen reduction reaction rate, it can be useful to compare the Co content in the particle-free zones of the surface, which should be actively participating in the oxygen reduction reaction. As seen in Figure 6 (c) and (d), the estimated Sr/Co composition ratio is higher for LSC50 in comparison to that on LSC25, with 8.5 and 4.6 for LSC50 and LSC25, respectively. From this finding, we can say that the excess Sr at the film surface is present not only as phase-separated particles (which can be up to tens of nm high (Figure S7 and Figure 6)) but also on the seemingly particle-free zones. Furthermore, the calculated average Co/(Sr+La) within the particle-free zones on LSC25 was 0.09, almost twice higher than 0.05 on LSC50. This ratio tells us that the amount of Co exposed at these particle-free zones at the surface (where ORR takes place) is more on the LSC25 compared to that on the LSC50 films. This is also consistent with the presence of more

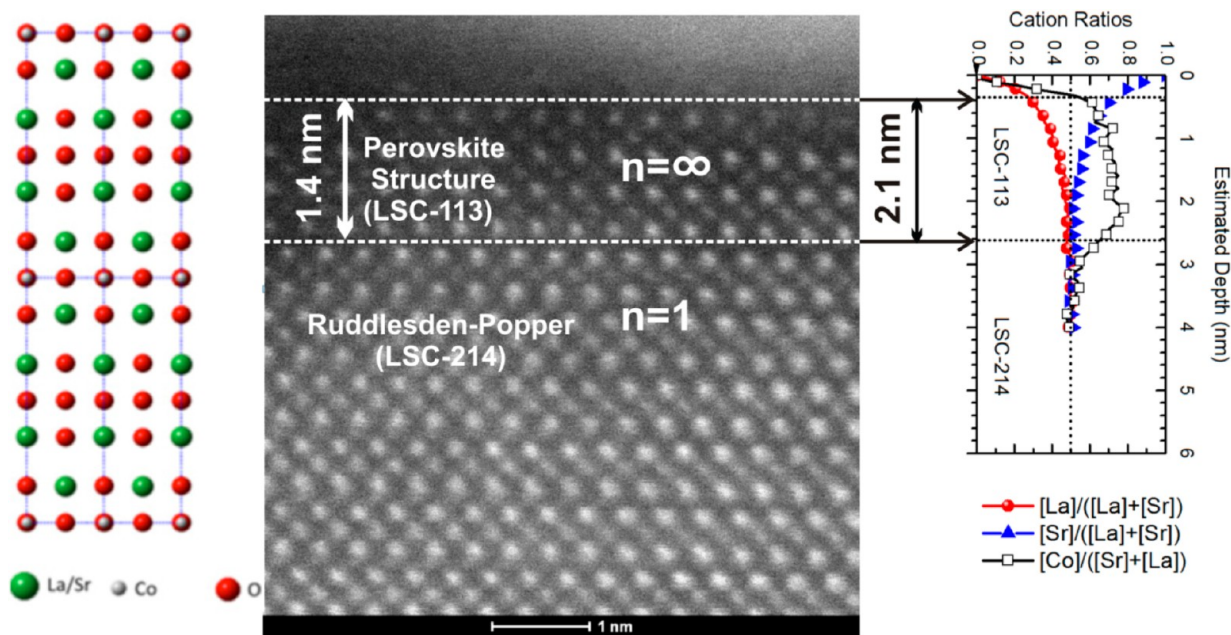


Figure 7. HAADF-STEM image of the cross-section of the near-surface region of the as-prepared LSC50 (001) (~ 80 nm thickness), aligned with an atomic structure rendering on the left and with the cation compositions obtained for the same film in the same depth zone by LEIS on the right. LEIS shows a Co enriched region near the surface, consistent with the $n = \infty$ stacking that gives LSC-113 perovskite as detected in STEM.

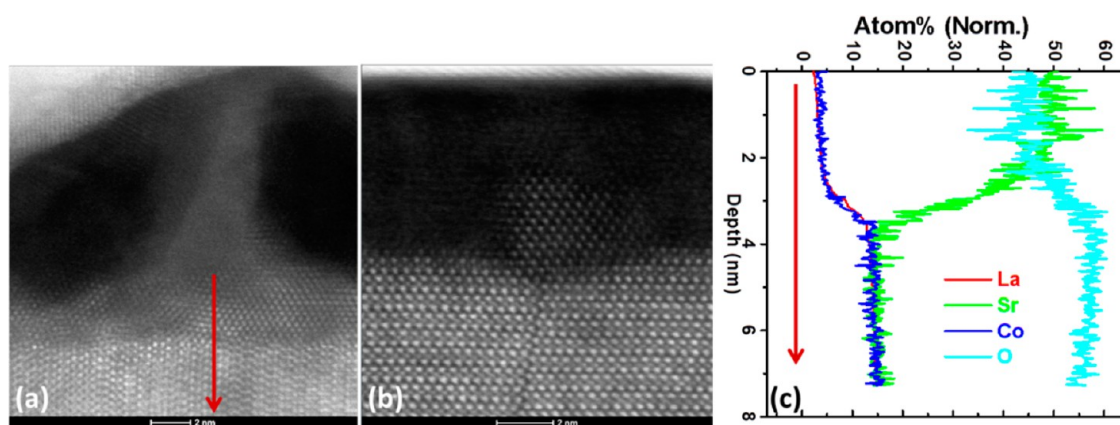


Figure 8. (a–b) Representative HAADF-STEM images of particles, likely of SrO_2 structure, at the surface (a) of LSC50 (100) and (b) of LSC50 (001). (c) A normalized EDS composition profile across the particle and LSC50 (100) film from image (a).

Co detected by LEIS at the outermost surface of LSC25 films compared to that on LSC50 for both the (100) and (001) orientations (see Figure 5 bar charts). Given the importance of the transition metal cations for oxygen reduction at oxide surfaces,^{49–51} this difference can be critical in determining the relative oxygen exchange kinetics at the LSC25 and LSC50 surfaces and will be discussed further in section 3.4.

3.2.3. Near-Surface Atomic Structure and Composition by STEM and EDS. Most of the LSC25 and LSC50 films with the (001) and (100) orientations showed a perfect stacking sequence of the 214 R–P phase (Figure 2 (c–d)) except from two types of anomalous structures observed at the surface. In summary, STEM and LEIS together identified the existence of a perovskite layer at the near surface of the 214 R–P films. Furthermore, this is the first time that the structure and chemistry of the Sr-rich particles at the segregated surfaces of perovskite and R–P related phases have been observed with atomic resolution by STEM and EDX. While our preliminary results suggest that the particles are most likely SrO_2 , the precise identification of the phase of these particles warrants further investigation. The detailed explanation of these findings follows below.

The first anomalous structure found is the perovskite blocks close to the surface of the LSC25 and LSC50 thin films in both the as-prepared and annealed materials. Figure 7 is a representative HAADF-STEM image on [100] (or [010]) zone of the thick LSC50 (001) film top surface. La ($Z = 57$) and Sr ($Z = 38$) atoms share the same site in the R–P phase, and both have a larger atomic number than Co ($Z = 27$). Therefore, La and Sr atomic columns exhibit the greatest intensities in the image, and the Co/O mixed atomic columns have intermediate intensities. Comparing the schematic atomic structure in Figure 7 with the HAADF-STEM image (and also with Figure 2) reveals that most of the film exhibits the 214 R–P structures. However, in the near surface region, the top 1–2 nm of the film (indicated by the arrow) is made up of three perovskite unit cells ($n = \infty$, LSC-113) rather than the 214 R–P structure ($n = 1$). Such perovskite structure at the near surface is consistent with the Co enriched region observed in LEIS depth profile measurements, as also recalled in Figure 7 right-most panel.

The second type of anomalous structure that was observed in all samples was the particles sitting at the surface. We believe these particles are the same as those observed by AFM (see Figure S4 and Figure 5). The particles on the surface of the

films exhibit a completely different structure than both the R–P and the perovskite phases. On the zone axis orientation that reveals the cubic structure in the majority of the film, the particle structure shows a quasi-hexagonal arrangement of bright intensities. The arrangement of the bright intensities is not strictly hexagonal. This could be a true characteristic of the structure but was compounded by sample drift during image acquisition, as evidenced by the slightly distorted lattice of the bulk film. Figure 8 (a–b) shows a typical morphology where such particles are usually observed. The dome structure capped by the Au layer has dark regions that are separated by an extended structure from the particles reaching to the top of the dome. Occasionally the particle was also observed to form at the top surface where a fault boundary terminates, shown in Figure 8 (b).

EDS analysis shows that the dark regions are characterized by extremely low X-ray counts, suggesting the dark region is very thin. Figure 8 (c) shows that when using the aforementioned internal standard for EDS quantification, the particle is composed almost entirely of Sr and O, with a ratio of Sr/O close to 1. One obvious possibility is that the particle could be SrO , and it was imaged on the $\langle 111 \rangle$ zone axis giving rise to the hexagonal arrangement of intensities in the STEM image. However, the measured distance between the nearest bright intensities for the particle is about 0.4 nm, whereas the corresponding spacing calculated from the SrO structure would be 0.21 nm. Therefore, the particle is not likely to be of the SrO structure.

We examined a number of Sr and O containing compounds to see if they match with the particle structure observed in Figure 8. The absence of C, N, and S peaks in the EDS ruled out compounds like SrCO_3 , $\text{Sr}(\text{NO}_3)_2$, and SrSO_4 . $\text{Sr}(\text{OH})_2$ was ruled out since the orthorhombic unit cell cannot produce the intensities with quasi-hexagonal symmetry. We concluded that the most likely identity of the particle is SrO_2 . The [100] or [010] zone of the SrO_2 structure can reproduce the intensities of the quasi-hexagonal symmetry. The spacing between the Sr rich columns on this zone is 0.35 or 0.4 nm, qualitatively consistent with the measured value. While the ratio of Sr/O for SrO_2 does not agree with the measured value, it should be noted that the measured compositions are based on an untested assumption that the bulk film has the strict stoichiometry of $(\text{La}_{0.5}\text{Sr}_{0.5})_2\text{CoO}_4$. Furthermore, particles have been observed to shrink/decompose under electron beam, which could skew the measured O composition (Figure S6).

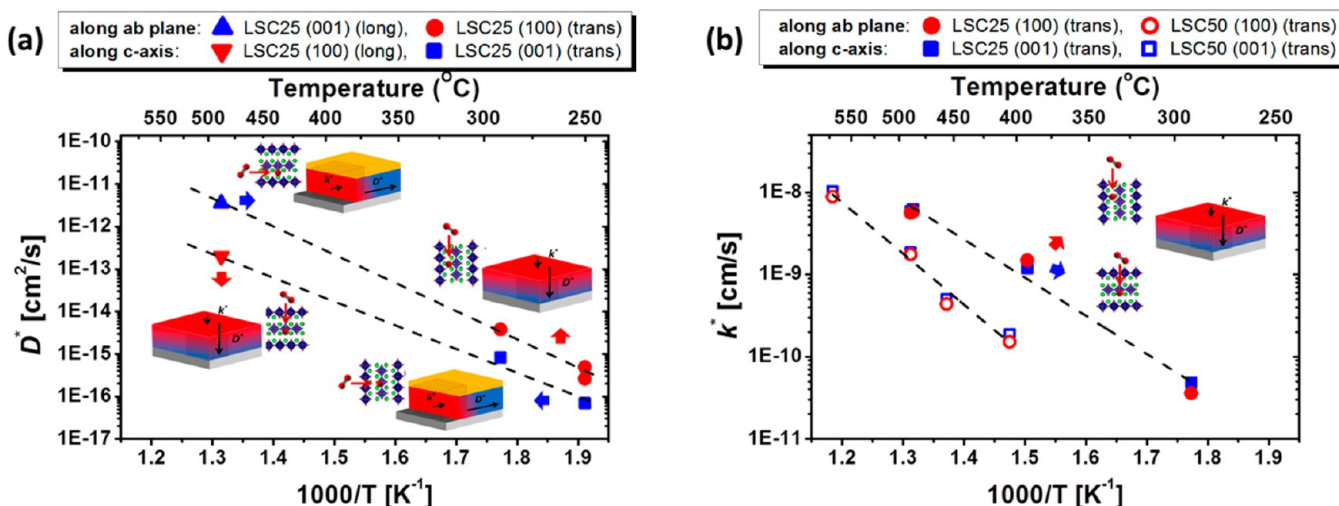


Figure 9. (a) Oxygen tracer diffusion coefficient D^* in LSC25, along the *ab*-plane (blue up triangles and red circles) and along the *c*-axis (red down triangles and blue squares) at different temperatures measured either in longitudinal configuration (long) or in the transverse configuration (trans) on LSC25 (001) or LSC25 (100) films (dashed lines are only guide to the eye). (b) The surface exchange coefficients, k^* , for LSC25 (001) films (closed blue squares), LSC25 (100) films (closed red circles), LSC50 (001) films (open blue squares), and LSC50 (100) films (open red circles) (dashed lines are only guide to the eye).

It is worth noting that our experiments were carried out at temperatures up to 500 °C in oxygen without the presence of water vapor. Previous thermodynamic analysis of Sr-oxide phases have shown that under these conditions SrO₂ is stable.⁶⁵ At higher temperatures (>527 °C)⁶⁵ or in the presence of water and CO₂, the SrO₂ may decompose into SrO or convert to Sr(OH)₂ or SrCoO₃.^{19,21,27} From a defect chemistry perspective, SrO₂ was also suggested to be the likely Sr-oxide in previous work examining the surface segregation phase on (La,Sr)(Co,Fe)O₃.¹⁴

3.3. Surface Exchange and Diffusion Kinetics.

3.3.1. Anisotropic Diffusion Kinetics of Oxygen Quantified by ¹⁸O SIMS Analysis. In order to evaluate the tracer oxygen diffusion coefficient (D^*) of the LSC50 films, we carried out ¹⁸O exchange on the relatively thick films (81–84 nm) at 500 °C. The normalized oxygen diffusion profiles obtained through the thick films after the ¹⁸O exchange for the 85 min are shown in Figure S8(a).

The surface exchange coefficients (k^*) extracted from the fit are very similar: 1.94×10^{-9} cm/s and 1.72×10^{-9} cm/s for LSC50 (100) and LSC50 (001), respectively. On the other hand, we found a large difference for the oxygen diffusion coefficient among the two different orientations: 1.20×10^{-13} cm²/s and 2.97×10^{-14} cm²/s for LSC50 (100) and LSC50 (001), respectively. As these measurements were carried out in the transverse configuration which limits the accuracy of the determination of the diffusion coefficient, it can be tentatively concluded that the oxygen diffusivity along the *ab*-planes of the LSC50 is at least 4 times faster than along the *c*-axis (Table S1).

In the case of the LSC25 films, an isotopic exchange at approximately 500 °C was carried out on thin films (45 nm) in the longitudinal configuration. The normalized oxygen tracer diffusion profiles obtained along the film (from trench, parallel to the film plane) after the of 65 h exchange are shown in Figure S8(b). The calculated D^* and k^* values are 3.58×10^{-12} cm²/s and 5.62×10^{-10} cm/s for LSC25 (001) and 1.99×10^{-13} cm²/s and 2.93×10^{-10} cm/s LSC25 (100), respectively. As these measurements were carried out in the longitudinal configuration we conclude that the oxygen diffusivity along the

ab-plane of the LSC25 (100) is almost 20 times faster than along the *c*-axis (Table S1). Anisotropic oxygen diffusion along the 2 main crystallographic directions (*ab*-plane and *c*-axis) were measured for LSC25 between 250 and 500 °C in both the transversal and longitudinal configurations (Figure 9(a)). The large difference in oxygen diffusivity between the two orientations in this composition is consistent with the previous computational predictions which showed an interstitial oxygen transport via an interstitialcy mechanism within the *ab*-plane.^{34,44,47,48}

3.3.2. Orientation “Independent” Surface Exchange Kinetics of Oxygen Quantified by ¹⁸O SIMS Analysis. We assessed the surface oxygen exchange kinetics on the thin LSC50 and LSC25 films (thickness of 39–45 nm) with two different orientations ((001) and (100)) by exchanging them in ¹⁸O at 290 to 575 °C and by measuring the ¹⁸O profile in the transverse configuration. We then fitted the normalized oxygen isotope fraction obtained to the plane-sheet solution. At the highest temperatures flat or almost-flat diffusion profiles were obtained. Due to the thinness of the films and to the different oxygen diffusion behavior in the top surface region (approximately 5 nm), it has not been possible to extract reliable oxygen diffusion coefficients from these thin films, and only the surface exchange coefficients were quantified. Figure 9(b) shows the temperature-activated behavior of the k^* . It is clear that for all the range of temperatures measured, the oxygen exchange kinetics is not orientation dependent, as there are no major differences between the (001) and (100) films. From these results, we can conclude that the segregated surface chemistry overrides the crystal anisotropy for both the LSC50 and LSC25 films. However, a clear difference in the surface exchange coefficients is observed when the composition is changed; by decreasing the Sr content from 50 to 25% an increase of approximately 3.5–8 times higher k^* has been measured in the 400–500 °C temperature range.

3.4. Discussion on Surface Chemistry and on Comparison of Surface Techniques. **3.4.1. Lack of Anisotropy in k^* on LSC25 and LSC50 and Dependence of D^* and k^* on Sr Doping Level.** As shown in the ¹⁸O SIMS

analyses (Figure 9(a) and Table S1), LSC25 and LSC50 films presented anisotropic oxygen diffusion kinetics, with the *ab*-plane diffusion being 4 and 20 times faster than the *c*-axis diffusion for the LSC50 and the LSC25 films, respectively. As reviewed in the introduction section, the main reason for the faster oxygen diffusion along the *ab*-plane in the 214 RP phase structure is the preferential migration via interstitialcy mechanism within the *ab*-plane. The increase of the Sr dopant level at the A-site changes the oxygen defect chemistry of the LSC films, by decreasing the oxygen interstitial concentration and by increasing the oxygen vacancy concentration.^{34,35,66} At 50% Sr doping, as in LSC50, the concentration of both the interstitials and vacancies is expected to be very low. This decrease in the oxygen interstitial content should then lower the diffusion coefficient D^* for the 214 LSC films by reducing the carrier concentration. Our finding of lower D^* for LSC50 films compared to the LSC25 is consistent with this expectation (Section 3.3.1) and also as shown previously for $(\text{La}_{1-x}\text{Sr}_x)_2\text{NiO}_4$ thin films.⁶⁷

On the other hand, the crystal orientation had no significant effect on the oxygen surface exchange kinetics (Figure 9(b)), contrary to previous theoretical predictions.³⁴ Both the LSC25 and LSC50 (001) films on STO had similar oxygen exchange coefficient as the (100) films on SLAO. We believe that the reason behind this lack of crystal termination dependence of the oxygen exchange kinetics at the surface is the Sr segregation. Han et al. theoretical results pointed out that the expected anisotropic oxygen exchange kinetics of La_2CoO_4 and LSC50 was mainly due to the anisotropically strong adsorption of O_2 onto the (100) surface compared to the (001) surface of the 214 RP structure.³⁴ Our HRXRD and STEM measurements demonstrated that the bulk of our LSC films have indeed the (001) and (100) orientations. However, we found by LEIS, XPS, AFM, AES, and STEM that the surfaces of these LSC films do not terminate with a structure that matches to the (100) and (001) planes of the 214 RP crystal lattice. The surface and near surface of the (100) and (001) films for each Sr doping level are very similar in composition and structure, with Sr segregation and phase separation at the top surface and a Co enriched layer beneath the surface (see sections 3.1 and 3.2). The phase separated Sr-rich surface layer is known to be detrimental to the oxygen reduction reactivity on perovskite oxide cathodes.^{21,27} In this work, the presence of a segregated surface seems to have overridden the differences expected in the oxygen absorption on the (100) and (001) surfaces of the 214 LSC films and led to similar oxygen exchange coefficients at the surface of the (001) and (100) orientations for both the LSC25 and the LSC50 compositions.

Although the oxygen exchange kinetics presented no dependence on crystal orientation, it clearly depends on the Sr dopant level in the bulk, namely 25% and 50% in this work. The surface exchange coefficient for LSC25 was 3.5 to 8 times higher than that for LSC50 in the 400–500 °C temperature range. To explain this composition dependence, we first look at the changes of LSC thin film bulk characteristics introduced by the increase of Sr dopant level. Doped LSC films with higher Sr were reported to enhance the electronic conductivity,⁶⁸ which might have a positive impact on the electron transfer process in oxygen reduction reaction. On the other hand, Han et al. first-principles based calculations suggest that doping of Sr into LSC hinders the oxygen adsorption and incorporation process relative to the undoped LSC due to structural reasons at the surface.³⁴ Furthermore, similarly to our argument for the Sr

composition dependence of D^* , the ability of the material to accommodate oxygen interstitials is also important for k^* . When the interstitial capacity of the LSC 214 reduces (from 25% to 50% Sr doping level), it is reasonable to expect that this reduction also makes it harder to incorporate oxygen interstitials into the lattice from the surface.

Furthermore, we observed differences in the coverage of the Sr-rich particles and the composition of the particle-free zones among the LSC25 and LSC50 films. A larger coverage of such particles on the surface of LSC50 (see Figure S5) on both orientations could be one reason for finding a smaller oxygen exchange coefficient, k^* , on LSC50 than that on LSC25. Interestingly, the Co/(La+Sr) ratio at the particle-free zones of the surface (where presumably the oxygen exchange takes place) was two times lower on LSC50 compared to that on LSC25, based on our nanoprobe AES analysis (see Figure 6). The Co/(La+Sr) ratio of the outmost surface quantified by LEIS was also found to be smaller on LSC50 than on LSC25 for both orientations (see Figure 4). B-site cations are known to be the active sites for oxygen reduction due to the preferential adsorption of oxygen on them, as shown on $(\text{La,Sr})_2\text{CoO}_4$,³⁴ La_2NiO_4 ,⁴⁹ $(\text{La,Sr})\text{MnO}_3$,^{50,51} and other perovskite oxides.⁵² We believe that the lower concentration of the electrochemically active Co cations exposed to the gas phase on LSC50 leads to a slower oxygen exchange kinetics by presenting less adsorption sites for oxygen gas at the surface compared to that on LSC25. The (100) and (001) surfaces (for each composition, LSC25 and LSC50) were found to have similar Co content at the top surface, leading to a similar amount of activate sites present for the oxygen exchange process. We also did not find significant difference in the oxidation states between the (100) and (001) films at the experimental condition of this work (Supporting Information Figure S9). These lead to no clear difference in k^* for LSC films with different orientations for a given Sr doping level but a clear dependence of k^* on Sr doping for a given orientation.

The segregated surfaces shown in this work are far from the traditionally recognized, ideally faceted surfaces of single crystal oxides. Considering that the surface composition is completely different than the bulk, faceting effects which discussed extensively for single crystal oxides are irrelevant to the point. Even with slight faceting, our key conclusion would be the same: the segregated chemistry and structure at the surface overrides the effect of crystallography on oxygen exchange kinetics; regardless of whether that crystallography effect is due the crystal anisotropy or the different facets exposed.

3.4.2. Techniques for Characterizing the Oxide Surface Composition and Structure. As seen in Results, the surface of the LSC films presents strong heterogeneities in three dimensions, laterally and in depth from the surface, in response to the preparation and annealing environments. This is typical of other perovskite and related compounds as reviewed in the Introduction section. We brought together several complementary characterization techniques to identify the atomistic details of this chemical and structural heterogeneity. We present a brief comparison of the information obtained by these techniques and their complementarity features in this section. We used XPS and LEIS to obtain the elemental composition with depth resolution from the surface. LEIS is a unique technique that can provide chemical composition from the outermost monolayer of the surface. The combination of LEIS with sputtering enabled us to capture the Sr enrichment at the top surface and the presence of a Co enriched layer beneath the

surface. XPS has a coarser depth resolution compared with LEIS but is capable of extracting depth dependent information by changing the photoemission angle in a nondestructive manner. Qualitatively both of the LEIS and XPS presented similar findings on the segregated LSC25 and LSC50 surfaces as discussed in section 3.1.3. XPS and LEIS are laterally averaging techniques and do not have the lateral resolution needed to detect the chemical heterogeneities at the surface. The nanoprobe AES, on the other hand, has provided us with the high lateral resolution (~ 10 nm) needed in mapping out the distribution of the phase-separated particles at the LSC25 and LSC50 surfaces. Using AES and AFM, we were able to identify the particles on the surface to be an Sr-enriched phase and also pointed to the different levels of Co presence at the particle-free zones of the LSC25 and LSC50 surfaces. This information was helpful in deducing the dependence of k^* on the Sr doping level. STEM and EDX enabled the atomic resolution visualization in structure and chemistry near the surface of the LSC films. By combining the STEM image with LEIS depth profiles, we were able to confirm the existence of a Co enriched subsurface in the perovskite structure ($n = \infty$ RP phase) near the surface. The STEM image of the atomic structure together with the local composition quantified by EDS indicated that the secondary phase particles at the surface are Sr-oxide based, consistent with the AES results, and furthermore pointed out that the particles were likely to be SrO_2 . It is encouraging that all the results obtained in this paper are consistent among the different techniques which themselves have different resolutions and limitations. The depth of information that we could obtain on the rich heterogeneities at the surface of the LSC films is thanks to the complementary nature of the palette of techniques we have used.

4. SUMMARY AND CONCLUSION

We assessed the surface chemistry and structure of the 214 RP phase LSC25 and LSC50 epitaxial thin films with (001) and (100) crystallographic orientations with respect to the oxygen surface exchange kinetics on them. Our LEIS and XPS analyses showed the formation of a Sr-enriched layer at the top surface of the as-prepared LSC25 and LSC50 films with both the (001) and (100) orientations. After annealing up to 500 °C in O_2 , the Sr-enrichment on the top surface further increased, leading to the clustering of Sr-rich secondary phase particles, as confirmed by AFM, AES, and STEM/EDS. These clusters are thought to be inactive to oxygen exchange reactions and partially block the surface, while also changing the composition of the particle-free regions of the LSC surface. Depth profiling of composition with LEIS together with the atomic resolution images obtained by STEM demonstrated the existence of a Co enriched layer beneath the surface in the perovskite structure ($n = \infty$ RP phases). We found that the oxygen diffusion coefficient, D^* , along the ab -plane is 4 times and 20 times higher compared to that along the c -axis for LSC50 and LSC25, respectively, based on our ^{18}O exchange and SIMS analyses at 400–500 °C. However, the surface oxygen exchange kinetic coefficient, k^* , did not show any dependence on the crystal orientation of the films. This insensitivity of k^* to crystal orientation of the film indicates that the strong Sr segregation at the surface overrides the effect of the structural anisotropy that was also expected for the surface exchange kinetics. On the other hand, k^* clearly depended on the Sr dopant level in the bulk, with 3.5–8 times faster oxygen surface exchange for LSC25 than that for LSC50 at 400–500 °C. We propose two key reasons for this behavior.

First is the greater ability of the LSC25 to incorporate and equilibrate oxygen interstitials in its bulk compared to LSC50. The second is the relatively larger concentration of the electrochemically active Co sites at the particle-free zones of the LSC25 surface compared to that on the LSC50 surface, as determined by AES and LEIS. The importance of surface chemistry here dominates over the strong effect of crystal anisotropy that was theoretically expected on the surface reactions. The results of this work demonstrate the critical role of surface chemistry in determining the oxygen exchange kinetics on perovskite and related complex oxides, for applications such as high temperature electrochemical energy conversion devices, oxygen separation ion transport membranes, redox based resistive switching memories, and sensors.

■ ASSOCIATED CONTENT

Supporting Information

S1: surface cleaning procedure before LEIS measurement, S2: isotopic exchange depth profiling experiments; S3: LEIS surface spectra; S4: LEIS depth profiling for thick LSC samples; S5: surface structure characterized by AFM; S6: interaction of Sr-rich particles with electron beam; S7: lateral heterogeneity in surface cation composition detected by AES; S8: diffusion kinetics of oxygen quantified by ^{18}O SIMS analysis. S9: Co oxidation state probed by XPS. The Supporting Information is available free of charge on the ACS Publications website at DOI: 10.1021/acs.chemmater.5b02292.

■ AUTHOR INFORMATION

Corresponding Authors

*E-mail: byildiz@mit.edu (B.Y.).

*E-mail: j.kilner@imperial.ac.uk (J.A.K.).

Present Address

[¶]Laboratoire des Matériaux et du Génie Physique (LMGP), UMR 5628 CNRS – Grenoble INPMinatéc 3, Parvis Louis Néel CS 50257, 38016 GRENOBLE Cedex 1 France.

Author Contributions

[#]These three authors contributed equally.

Notes

The authors declare no competing financial interest.

■ ACKNOWLEDGMENTS

Y.C., N.T., Z.C., and B.Y. thank the Tsinghua-MIT-Cambridge Alliance and the USDOE Basic Energy Sciences (Grant No. DE-SC0002633) for financial support. Y.C. acknowledges support from the Schlumberger Foundation Faculty for the Future fellowship. H.T. and M.B. acknowledge funding from the 7th European Community Framework Programme of the European Union (Marie Curie Intra European fellowships: PIEF-GA-2010-274999 and PIEF-GA-2009-252711, respectively). This work made use of the MRSEC Shared Experimental Facilities at MIT, supported by the National Science Foundation under award number DMR-1419807. D.W.M. acknowledges support from The Ohio Third Frontier Program through an Ohio Research Scholar award. The authors gratefully acknowledge Prof. Tatsumi Ishihara and Dr. John Druce for supporting the LEIS experiments performed at wpi-12CNER (Kyushu University).

■ REFERENCES

(1) Kuklja, M. M.; Kotomin, E. A.; Merkle, R.; Mastrikov, Y. A.; Maier, J. Combined theoretical and experimental analysis of processes

determining cathode performance in solid oxide fuel cells. *Phys. Chem. Chem. Phys.* **2013**, *15* (15), 5443–5471.

(2) Laguna-Bercero, M. A. Recent advances in high temperature electrolysis using solid oxide fuel cells: A review. *J. Power Sources* **2012**, *203*, 4–16.

(3) Kilner, J. A.; Burriel, M. Materials for Intermediate-Temperature Solid-Oxide Fuel Cells. *Annu. Rev. Mater. Res.* **2014**, *44* (1), 365–393.

(4) Habib, M. A.; Nemitallah, M.; Ben-Mansour, R. Recent Development in Oxy-Combustion Technology and Its Applications to Gas Turbine Combustors and ITM Reactors. *Energy Fuels* **2013**, *27* (1), 2–19.

(5) Adler, S. B.; Lane, J. A.; Steele, B. C. H. Electrode Kinetics of Porous Mixed - Conducting Oxygen Electrodes. *J. Electrochem. Soc.* **1996**, *143* (11), 3554.

(6) Waser, R.; Aono, M. Nanoionics-based resistive switching memories. *Nat. Mater.* **2007**, *6* (11), 833–840.

(7) Waser, R.; Dittmann, R.; Staikov, G.; Szot, K. Redox-Based Resistive Switching Memories - Nanoionic Mechanisms, Prospects, and Challenges. *Adv. Mater.* **2009**, *21* (25–26), 2632.

(8) Kilner, J. A.; Berenov, A.; Rossiny, J. Diffusivity of the Oxide ion in Perovskite Oxides. In *Perovskite Oxide for Solid Oxide Fuel Cells*; Ishihara, T., Ed.; Springer: 2009; pp 95–116.

(9) Merkle, R.; Maier, J.; Bouwmeester, H. J. M. A linear free energy relationship for gas-solid interactions: Correlation between surface rate constant and diffusion coefficient of oxygen tracer exchange for electron-rich perovskites. *Angew. Chem., Int. Ed.* **2004**, *43* (38), 5069–5073.

(10) De Souza, R. A. A universal empirical expression for the isotope surface exchange coefficients (k^*) of acceptor-doped perovskite and fluorite oxides. *Phys. Chem. Chem. Phys.* **2006**, *8* (7), 890–897.

(11) Matrikov, Y. A.; Merkle, R.; Heifets, E.; Kotomin, E. A.; Maier, J. Pathways for Oxygen Incorporation in Mixed Conducting Perovskites: A DFT-Based Mechanistic Analysis for (La, Sr)MnO₃-delta. *J. Phys. Chem. C* **2010**, *114* (7), 3017–3027.

(12) Druce, J.; Ishihara, T.; Kilner, J. Surface composition of perovskite-type materials studied by Low Energy Ion Scattering (LEIS). *Solid State Ionics* **2014**, *262*, 893–896.

(13) Kreller, C. R.; McDonald, T. J.; Adler, S. B.; Crumlin, E. J.; Mutoro, E.; Ahn, S. J.; la O', G. J.; Shao-Horn, Y.; Biegalski, M. D.; Christen, H. M.; Chater, R. R.; Kilner, J. A. Origin of Enhanced Chemical Capacitance in La_{0.8}Sr_{0.2}CoO₃-delta Thin Film Electrodes. *J. Electrochem. Soc.* **2013**, *160* (9), F931–F942.

(14) Oh, D.; Gostovic, D.; Wachsmann, E. D. Mechanism of La_{0.6}Sr_{0.4}Co_{0.2}Fe_{0.8}O₃ cathode degradation. *J. Mater. Res.* **2012**, *27* (15), 1992–1999.

(15) Jung, W.; Tuller, H. L. Investigation of surface Sr segregation in model thin film solid oxide fuel cell perovskite electrodes. *Energy Environ. Sci.* **2012**, *5* (1), 5370–5378.

(16) Bucher, E.; Sitte, W.; Klauser, F.; Bertel, E. Impact of humid atmospheres on oxygen exchange properties, surface-near elemental composition, and surface morphology of La_{0.6}Sr_{0.4}CoO₃-delta. *Solid State Ionics* **2012**, *208* (0), 43–51.

(17) Joo, J. H.; Merkle, R.; Maier, J. Effects of water on oxygen surface exchange and degradation of mixed conducting perovskites. *J. Power Sources* **2011**, *196* (18), 7495–7499.

(18) Cai, Z. H.; Kuru, Y.; Han, J. W.; Chen, Y.; Yildiz, B. Surface Electronic Structure Transitions at High Temperature on Perovskite Oxides: The Case of Strained La_{0.8}Sr_{0.2}CoO₃ Thin Films. *J. Am. Chem. Soc.* **2011**, *133* (44), 17696–17704.

(19) Lee, W.; Han, J. W.; Chen, Y.; Cai, Z. H.; Yildiz, B. Cation Size Mismatch and Charge Interactions Drive Dopant Segregation at the Surfaces of Manganite Perovskites. *J. Am. Chem. Soc.* **2013**, *135* (21), 7909–7925.

(20) Kubicek, M.; Cai, Z. H.; Ma, W.; Yildiz, B.; Hutter, H.; Fleig, J. Tensile Lattice Strain Accelerates Oxygen Surface Exchange and Diffusion in La_{1-x}Sr_xCoO₃-delta Thin Films. *ACS Nano* **2013**, *7* (4), 3276–3286.

(21) Chen, Y.; Jung, W. C.; Kim, J. J.; Cai, Z.; Tuller, H. L.; Yildiz, B. Impact of Sr segregation on the electronic structure and oxygen

reduction activity of SrTi_{1-x}Fe_xO₃ surfaces. *Energy Environ. Sci.* **2012**, *5*, 7979.

(22) Chen, Y.; Jung, W. C.; Kuru, Y.; Tuller, H.; Yildiz, B. Chemical, Electronic and Nanostructure Dynamics on Sr(Ti_{1-x}Fe_x)O₃ Thin-Film Surfaces at High Temperatures. *Solid Oxide Fuel Cells 12 (Sofc Xii)* **2011**, *35* (1), 2409–2416.

(23) Ortiz-Vitoriano, N.; de Larramendi, I. R.; Cook, S. N.; Burriel, M.; Aguadero, A.; Kilner, J. A.; Rojo, T. The Formation of Performance Enhancing Pseudo-Composites in the Highly Active La_{1-x}CaxFe_{0.8}Ni_{0.2}O₃ System for IT-SOFC Application. *Adv. Funct. Mater.* **2013**, *23* (41), 5131–5139.

(24) Burriel, M.; Wilkins, S.; Hill, J. P.; Munoz-Marquez, M. A.; Brongersma, H. H.; Kilner, J. A.; Ryan, M. P.; Skinner, S. J. Absence of Ni on the outer surface of Sr doped La₂NiO₄ single crystals. *Energy Environ. Sci.* **2014**, *7* (1), 311–316.

(25) Kilner, J. A.; Tellez Lozano, H.; Burriel, M.; Cook, S.; Druce, J. The Application of Ion Beam Analysis to Mass Transport Studies in Mixed Electronic Ionic Conducting Electrodes. *ECS Trans.* **2013**, *57* (1), 1701–1708.

(26) Druce, J.; Tellez, H.; Burriel, M.; Sharp, M.; Fawcett, L.; Cook, S. N.; McPhail, D.; Ishihara, T.; Brongersma, H. H.; Kilner, J. A. Surface Termination and Subsurface Restructuring of Perovskite-based Solid Oxide Electrode Materials. *Energy Environ. Sci.* **2014**, *7* (11), 3593–3599.

(27) Cai, Z. H.; Kubicek, M.; Fleig, J.; Yildiz, B. Chemical Heterogeneities on La_{0.6}Sr_{0.4}CoO₃-delta Thin Films-Correlations to Cathode Surface Activity and Stability. *Chem. Mater.* **2012**, *24* (6), 1116–1127.

(28) Egger, A.; Sitte, W.; Klauser, F.; Bertel, E. Long-Term Oxygen Exchange Kinetics of Nd₂NiO₄ + delta in H₂O - and CO₂-Containing Atmospheres. *J. Electrochem. Soc.* **2010**, *157* (11), B1537–B1541.

(29) Tellez, H.; Druce, J.; Ju, Y.-W.; Kilner, J.; Ishihara, T. Surface Chemistry Evolution in LnBaCo₂O_{5+delta} Double Perovskites for Oxygen Electrodes. *Int. J. Hydrogen Energy* **2014**, *39*, 20856–20863.

(30) Sase, M.; Hermes, F.; Yashiro, K.; Sato, K.; Mizusaki, J.; Kawada, T.; Sakai, N.; Yokokawa, H. Enhancement of oxygen surface exchange at the hetero-interface of (La,Sr)CoO(3)/(La,Sr)(2)CoO(4) with PLD-Layered films. *J. Electrochem. Soc.* **2008**, *155* (8), B793–B797.

(31) Sase, M.; Hermes, F.; Yashiro, K.; Sato, K.; Mizusaki, J.; Kawada, T.; Sakai, N.; Yokokawa, H. Enhancement of oxygen surface exchange at the hetero-interface of (La,Sr)CoO3/(La,Sr)(2)CoO4 with PLD-Layered films. *J. Electrochem. Soc.* **2008**, *155* (8), B793–B797.

(32) Tarancon, M.; Burriel, M.; Santiso, J.; Skinner, S. J.; Kilner, J. A. Advances in Layered Oxide cathodes for intermediate temperature solid oxide fuel cells. *J. Mater. Chem.* **2010**, *20*, 3799–3813.

(33) Bassat, J. M.; Burriel, M.; Wahyudi, O.; Castaing, R.; Ceretti, M.; Veber, P.; Weill, I.; Villesuzanne, A.; Grenier, J. C.; Paulus, W.; Kilner, J. A. Anisotropic Oxygen Diffusion Properties in Pr₂NiO₄+delta and Nd₂NiO₄+delta Single Crystals. *J. Phys. Chem. C* **2013**, *117* (50), 26466–26472.

(34) Han, J. W.; Yildiz, B. Mechanism for enhanced oxygen reduction kinetics at the (La,Sr)CoO₃-delta/(La,Sr)(2)CoO₄+delta hetero-interface. *Energy Environ. Sci.* **2012**, *5* (9), 8598–8607.

(35) Vashook, V. V.; Ullmann, H.; Olshevskaya, O. P.; Kulik, V. P.; Lukashevich, V. E.; Kokhanovskij, L. V. Composition and electrical conductivity of some cobaltates of the type La(2-x)Sr(x)CoO(4.5-x/2+delta). *Solid State Ionics* **2000**, *138* (1–2), 99–104.

(36) Allan, N. L.; Mackrodt, W. C. Oxygen Ion Migration in La₂CuO₄. *Philos. Mag. A* **1991**, *64* (5), 1129–1132.

(37) Allan, N. L.; Lawton, J. M.; Mackrodt, W. C. A Comparison of the Calculated Lattice and Defect Structures of La₂CuO₄, La₂NiO₄, Nd₂CuO₄, Pr₂CuO₄, Y₂CuO₄, Al₂CuO₄ - Relationship to High-Tc Superconductivity. *Philos. Mag. B* **1989**, *59* (2), 191–206.

(38) Savvin, S. N.; Mazo, G. N.; Ivanov-Schitz, A. K. Simulation of ion transport in layered cuprates La₂-xSr_xCuO₄-delta. *Crystallogr. Rep.* **2008**, *53* (2), 291–301.

(39) Savvin, S. N.; Mazo, G. N.; Ivanov-Schitz, A. K. Oxygen diffusion in La₂-xSr_xCuO₄-delta: Molecular dynamics study. *Defect Diffus. Forum* **2005**, *242–244*, 27–42.

- (40) Mazo, G. N.; Savvin, S. N. The molecular dynamics study of oxygen mobility in $\text{La}_{2-x}\text{Sr}_x\text{CuO}_{4-\delta}$. *Solid State Ionics* **2004**, *175* (1–4), 371–374.
- (41) Mazo, G. N.; Savvin, S. N.; Petrykin, V. V.; Koudriashov, I. A. Oxygen mobility in layered cuprates $\text{La}_{2-x}\text{Sr}_x\text{CuO}_{4-\delta}$. *Solid State Ionics* **2001**, *141–142*, 313–319.
- (42) Minervini, L.; Grimes, R. W.; Kilner, J. A.; Sickafus, K. E. Oxygen migration in $\text{La}_2\text{NiO}_{4+\delta}$. *J. Mater. Chem.* **2000**, *10* (10), 2349–2354.
- (43) Cleave, A. R.; Kilner, J. A.; Skinner, S. J.; Murphy, S. T.; Grimes, R. W. Atomistic computer simulation of oxygen ion conduction mechanisms in La_2NiO_4 . *Solid State Ionics* **2008**, *179* (21–26), 823–826.
- (44) Kushima, A.; Parfitt, D.; Chroneos, A.; Yildiz, B.; Kilner, J. A.; Grimes, R. W. Interstitialcy diffusion of oxygen in tetragonal $\text{La}_2\text{CoO}_{4+\delta}$. *Phys. Chem. Chem. Phys.* **2011**, *13* (6), 2242–2249.
- (45) Parfitt, D.; Chroneos, A.; Kilner, J. A.; Grimes, R. W. Molecular dynamics study of oxygen diffusion in $\text{Pr}_2\text{NiO}_{4+\delta}$. *Phys. Chem. Chem. Phys.* **2010**, *12* (25), 6834–6836.
- (46) Chroneos, A.; Vovk, R. V.; Goulatis, I. L.; Goulatis, L. I. Oxygen transport in perovskite and related oxides: A brief review. *J. Alloys Compd.* **2010**, *494* (1–2), 190–195.
- (47) Chroneos, A.; Parfitt, D.; Kilner, J. A.; Grimes, R. W. Anisotropic oxygen diffusion in tetragonal $\text{La}_2\text{NiO}_{4+\delta}$: molecular dynamics calculations. *J. Mater. Chem.* **2010**, *20* (2), 266–270.
- (48) Tealdi, C.; Ferrara, C.; Mustarelli, P.; Islam, M. S. Vacancy and interstitial oxide ion migration in heavily doped $\text{La}_{2-x}\text{Sr}_x\text{CoO}_{4\pm\delta}$. *J. Mater. Chem.* **2012**, *22* (18), 8969–8975.
- (49) Zhou, J.; Chen, G.; Wu, K.; Cheng, Y. Interaction of La_2NiO_4 (100) Surface with Oxygen Molecule: A First-Principles Study. *J. Phys. Chem. C* **2013**, *117* (25), 12991–12999.
- (50) Chen, H. T.; Raghunath, P.; Lin, M. C. Computational Investigation of O₂ Reduction and Diffusion on 25% Sr-Doped LaMnO_3 Cathodes in Solid Oxide Fuel Cells. *Langmuir* **2011**, *27* (11), 6787–6793.
- (51) Choi, Y.; Lin, M. C.; Liu, M. L. Computational study on the catalytic mechanism of oxygen reduction on $\text{La}_{0.5}\text{Sr}_{0.5}\text{MnO}_3$ in solid oxide fuel cells. *Angew. Chem., Int. Ed.* **2007**, *46* (38), 7214–7219.
- (52) Lee, Y.-L.; Kleis, J.; Rossmeisl, J.; Morgan, D. Ab initio energetics of $\text{LaBO}_3(001)$ (B=Mn, Fe, Co, and Ni) for solid oxide fuel cell cathodes. *Phys. Rev. B: Condens. Matter Mater. Phys.* **2009**, *80* (22), 224101.
- (53) Claus, J.; Borchardt, G.; Weber, S.; Hiver, J. M.; Scherrer, S. Combination of EBSP measurements and SIMS to study crystallographic orientation dependence of diffusivities in a polycrystalline material: Oxygen tracer diffusion in $\text{La}_{2-x}\text{Sr}_x\text{CuO}_{4\pm\delta}$. *Mater. Sci. Eng., B* **1996**, *38* (3), 251–257.
- (54) Opila, E. J.; Tuller, H. L.; Wuensch, B. J.; Maier, J. OXYGEN TRACER DIFFUSION IN $\text{La}_{2-x}\text{Sr}_x\text{CuO}_{4-y}$ SINGLE-CRYSTALS. *J. Am. Ceram. Soc.* **1993**, *76* (9), 2363–2369.
- (55) Bassat, J. M.; Odier, P.; Villesuzanne, A.; Marin, C.; Pouchard, M. Anisotropic ionic transport properties in $\text{La}_2\text{NiO}_{4+\delta}$ single crystals. *Solid State Ionics* **2004**, *167* (3–4), 341–347.
- (56) Burriel, M.; Garcia, G.; Santiso, J.; Kilner, J. A.; Chater, R. J.; Skinner, S. J. Anisotropic oxygen diffusion properties in epitaxial thin films of $\text{La}_2\text{NiO}_{4+\delta}$. *J. Mater. Chem.* **2008**, *18* (4), 416–422.
- (57) Gauquelin, N. *Impact of the structural anisotropy of $\text{La}_2\text{NiO}_{4+\delta}$ on high temperature surface modification and diffusion of oxygen*; RWTH Aachen University: 2010.
- (58) Momma, K.; Izumi, F. VESTA 3 for three-dimensional visualization of crystal, volumetric and morphology data. *J. Appl. Crystallogr.* **2011**, *44*, 1272–1276.
- (59) Brongersma, H. H. Low-Energy Ion Scattering. In *Characterization of Materials*; Kaufmann, E. N., Ed.; John Wiley & Sons, Inc.: New York, 2012; pp 2024–2044.
- (60) Shin, H. H.; McIntosh, S. On the H_2/D_2 isotopic exchange rate of proton conducting barium cerates and zirconates. *J. Mater. Chem. A* **2013**, *1* (26), 7639–7647.
- (61) Kirkland, E. J.; Loane, R. F.; Silcox, J. SIMULATION OF ANNULAR DARK FIELD STEM IMAGES USING A MODIFIED MULTISLICE METHOD. *Ultramicroscopy* **1987**, *23* (1), 77–96.
- (62) Loane, R. F.; Xu, P.; Silcox, J. INCOHERENT IMAGING OF ZONE AXIS CRYSTALS WITH ADF STEM. *Ultramicroscopy* **1992**, *40* (2), 121–138.
- (63) Gauquelin, N.; Weirich, T.; Ceretti, M.; Paulus, W.; Schroeder, M. Long-term structural surface modifications of mixed conducting $\text{La}_2\text{NiO}_{4+\delta}$ at high temperatures. *Monatsh. Chem.* **2009**, *140* (9), 1095–1102.
- (64) Kubicek, M.; Fromling, T.; Hutter, H.; Fleig, J.; Limbeck, A. Relationship between Cation Segregation and the Electrochemical Oxygen Reduction Kinetics of $\text{La}_{0.6}\text{Sr}_{0.4}\text{CoO}_{3-\delta}$ Thin Film Electrodes. *J. Electrochem. Soc.* **2011**, *158* (6), B727–B734.
- (65) Middleburgh, S. C.; Lagerlof, K. P. D.; Grimes, R. W. Accommodation of Excess Oxygen in Group II Monoxides. *J. Am. Ceram. Soc.* **2013**, *96* (1), 308–311.
- (66) Nakamura, T.; Yashiro, K.; Sato, K.; Mizusaki, J. Oxygen nonstoichiometry and defect equilibrium in $\text{La}_{2-x}\text{Sr}_x\text{NiO}_{4+\delta}$. *Solid State Ionics* **2009**, *180* (4–5), 368–376.
- (67) Skinner, S. J.; Kilner, J. A. Oxygen diffusion and surface exchange in $\text{La}_{2-x}\text{Sr}_x\text{NiO}_{4+\delta}$. *Solid State Ionics* **2000**, *135* (1–4), 709–712.
- (68) Matsuura, T.; Tabuchi, J.; Mizusaki, J.; Yamauchi, S.; Fueki, K. ELECTRICAL-PROPERTIES OF $\text{La}_{2-x}\text{Sr}_x\text{CoO}_{4-\delta}$ 0.1. STRUCTURE, ELECTRICAL-CONDUCTIVITY, AND SEEBECK COEFFICIENT OF SINGLE-CRYSTALS (X = 0.0, 0.5, 1.0 AND 1.5). *J. Phys. Chem. Solids* **1988**, *49* (12), 1403–1408.